

Rashba effect and point-defect engineering synergistically improve the thermoelectric performance of the entropy-stabilized $\text{Sn}_{0.8}\text{Ge}_{0.2}\text{Te}_{0.8}\text{Se}_{0.2}$ alloy

Liangwei Fu,^{a,†,*} Kangpeng Jin,^{a,†} Dan Zhang,^b Chenghao Zhang,^a Haonan Nie,^a Zixiong Zhen,^a Pan Xiong,^a Ming Huang,^c Jiaqing He,^d Biao Xu^{a,*}

^a School of Chemistry and Chemical Engineering, Nanjing University of Science and Technology, Nanjing 210094, China

^b Key Laboratory of High-Precision Computation and Application of Quantum Field Theory of Hebei Province, College of Physics Science and Technology, Hebei University, Baoding 071002, China

^c School of Materials Science and Engineering, Nanjing University of Science and Technology, Nanjing 210094, China.

^d Shenzhen Key Laboratory of Thermoelectric Materials, Department of Physics, Southern University of Science and Technology, Shenzhen 518055, China

† These authors contributed to the work equally.

*Corresponding authors: fulw@njust.edu.cn (L.W.F.), xubiao@njust.edu.cn (B.X.)

Supplementary content

Section 1: Supplementary figures

Section 2: Supplementary tables

Section 3: Study on the mobility of $\text{SnTe}_{1-x}\text{Se}_x$ samples

Section 4: Density functional theory calculation.

Section 1: Supplementary figures

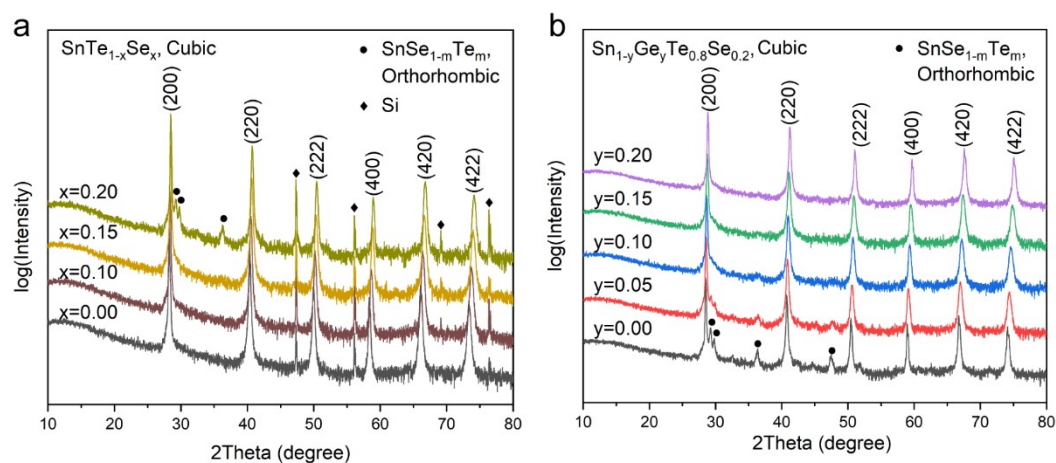


Fig. S1 The XRD patterns of $\text{SnTe}_{1-x}\text{Se}_x$ ($x = 0.00-0.20$) and $\text{Sn}_{1-y}\text{Ge}_y\text{Te}_{0.8}\text{Se}_{0.2}$ ($y = 0.00-0.20$) samples. The Si powders in $\text{SnTe}_{1-x}\text{Se}_x$ samples are used as the standard.

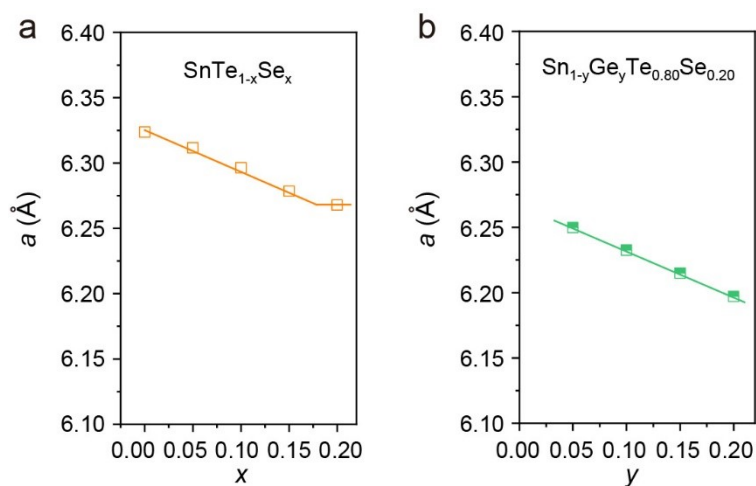


Fig. S2 The lattice parameters (a) of $\text{SnTe}_{1-x}\text{Se}_x$ ($x = 0.00, 0.05, 0.10, 0.15$ and 0.20) and $\text{Sn}_{1-y}\text{Ge}_y\text{Te}_{0.8}\text{Se}_{0.2}$ ($y = 0.05, 0.10, 0.15, 0.20$).

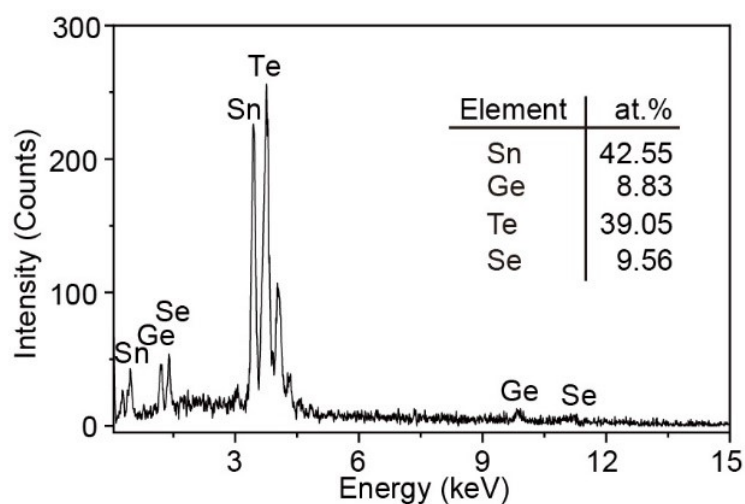


Fig. S3 The quantitative SEM-EDS result of $\text{Sn}_{0.8}\text{Ge}_{0.2}\text{Te}_{0.8}\text{Se}_{0.2}$

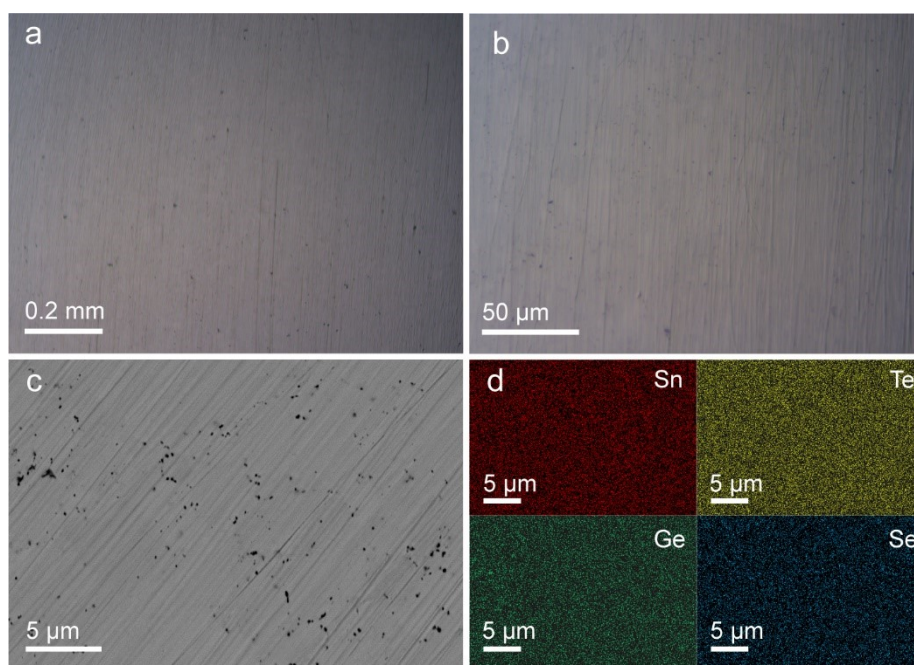


Fig. S4 (a) Low and (b) high magnified metallographic images for $\text{Sn}_{0.8}\text{Ge}_{0.2}\text{Te}_{0.8}\text{Se}_{0.2}$ sample. (c) The back-scattered electron image of the polished surface of $\text{Sn}_{0.8}\text{Ge}_{0.2}\text{Te}_{0.8}\text{Se}_{0.2}$ sample. The black region may be holes in the sample or holes caused by grinding and polishing. (d) EDS mapping of the polished surface of $\text{Sn}_{0.8}\text{Ge}_{0.2}\text{Te}_{0.8}\text{Se}_{0.2}$ sample.

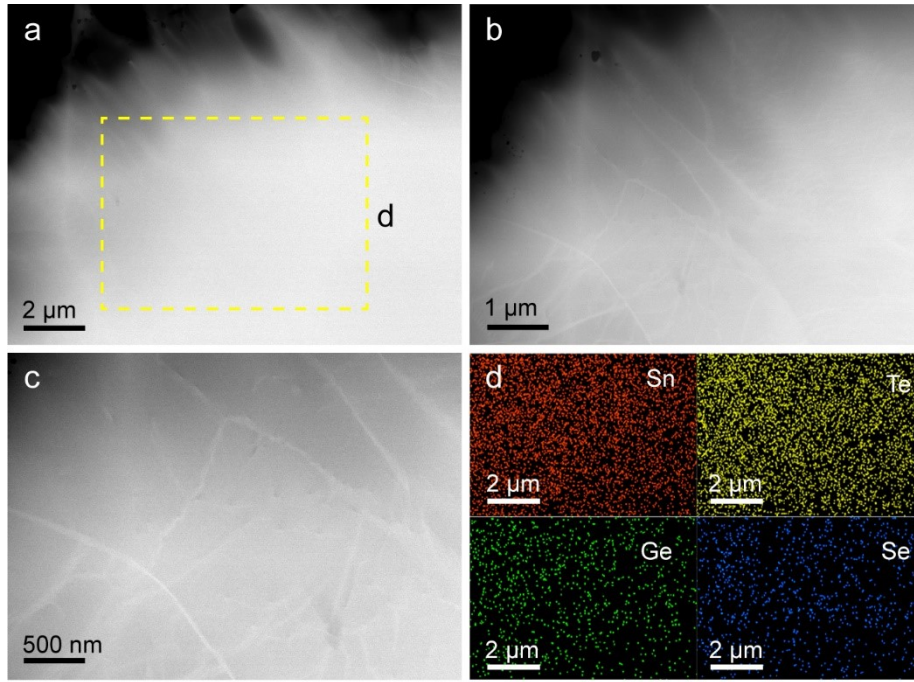


Fig. S5 (a)-(c) HAADF images for $\text{Sn}_{0.8}\text{Ge}_{0.2}\text{Te}_{0.8}\text{Se}_{0.2}$ sample. (d) EDS mapping of the $\text{Sn}_{0.8}\text{Ge}_{0.2}\text{Te}_{0.8}\text{Se}_{0.2}$ sample conducted on the region indicated in (a) by a yellow dash box.

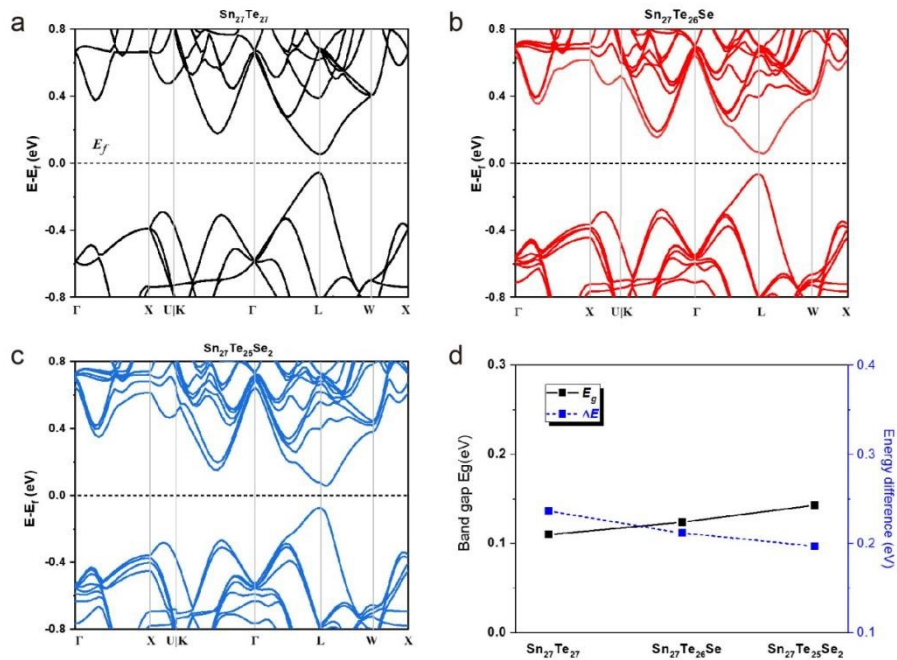


Fig. S6 (a-c) The band structure of $\text{Sn}_{27}\text{Te}_{27}$, $\text{Sn}_{27}\text{Te}_{26}\text{Se}$ and $\text{Sn}_{27}\text{Te}_{25}\text{Se}_2$. (d) The changes of band gap and energy difference with alloying Se in SnTe.

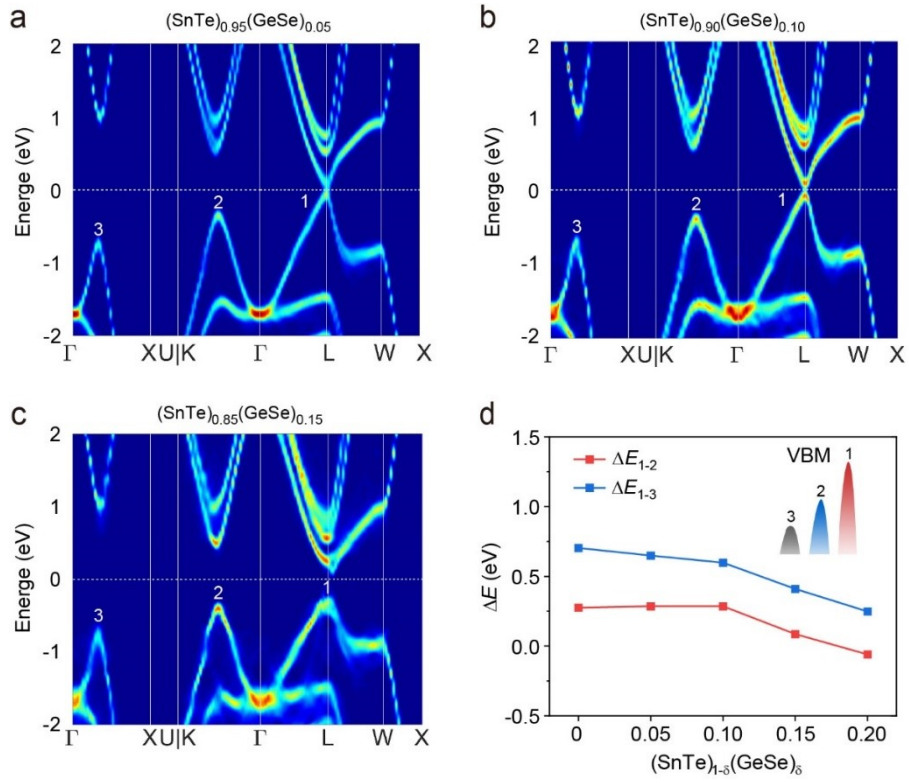


Fig. S7 (a-c) The band structure of $(\text{SnTe})_{1-\delta}(\text{GeSe})_{\delta}$ ($\delta = 0.05, 0.10, 0.15$). (d) The changes of energy offset between 1, 2 and 3 band near VBM.

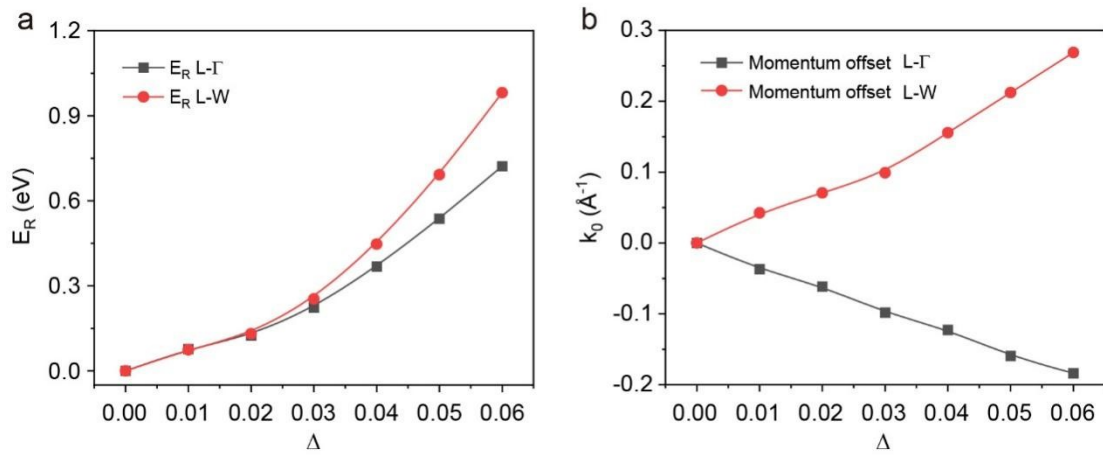


Fig. S8 Δ -dependent Rashba energy (E_R) and momentum offset (k_0).

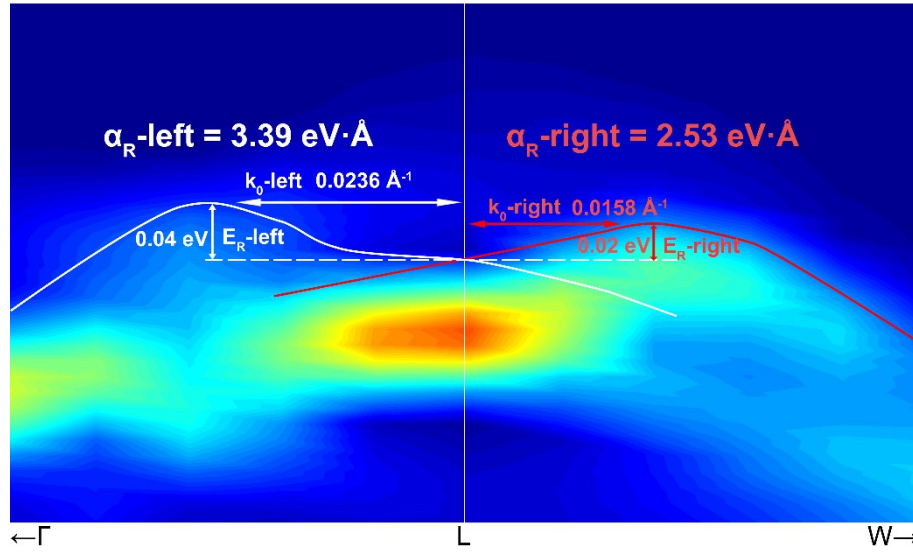


Fig. S9 The L band structure of $\text{Sn}_{0.8}\text{Ge}_{0.2}\text{Te}_{0.8}\text{Se}_{0.2}$ sample. The inset shows the meaning of Rashba energy (E_R) and momentum offset (k_0).

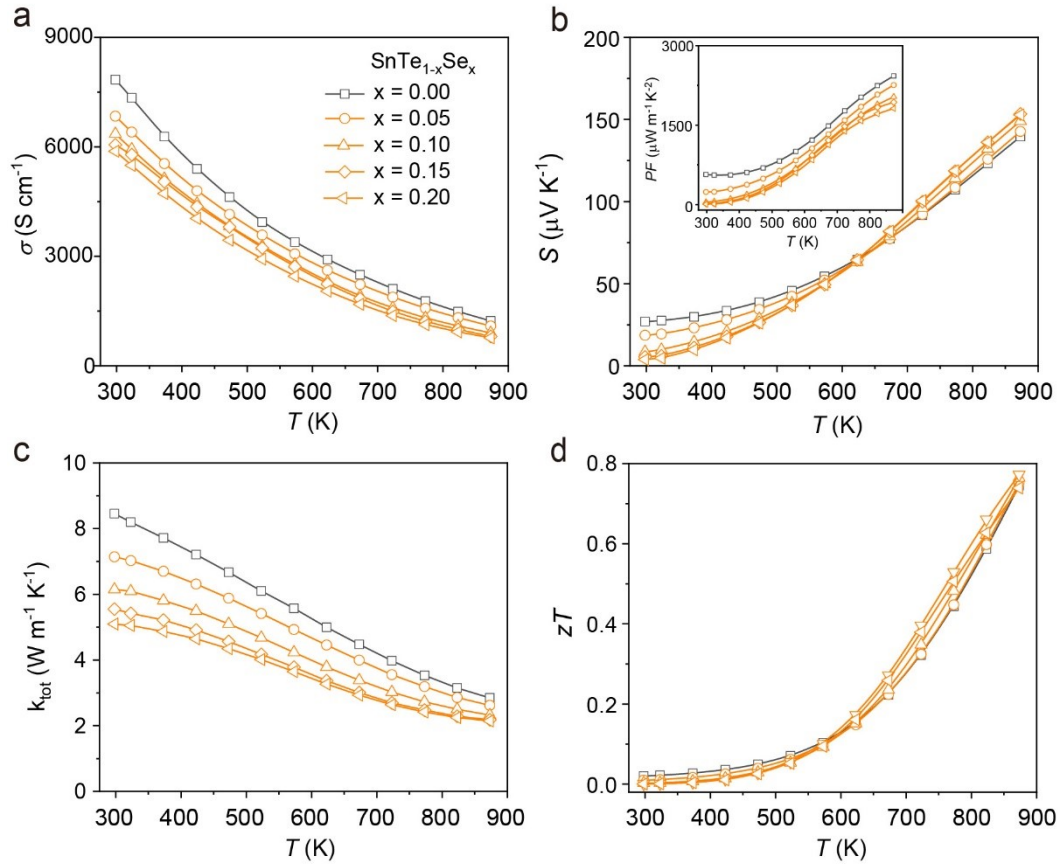


Fig. S10 T -dependent thermoelectric properties of $\text{SnTe}_{1-x}\text{Se}_x$ ($x = 0.00, 0.05, 0.10, 0.15, 0.20$) samples: (a) Electrical conductivity, (b) Seebeck coefficient, (c) total thermal conductivity, and (d) zT value. The inset of b shows the T -dependent power

factor.

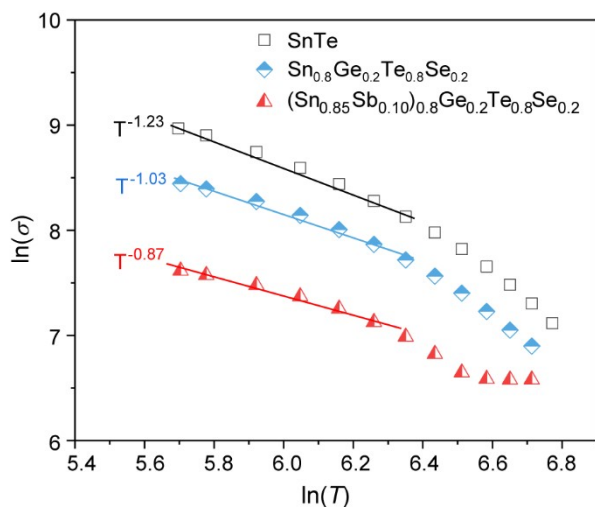


Fig. S11 The plot of $\ln(\sigma)$ versus $\ln(T)$ for SnTe, $\text{Sn}_{0.8}\text{Ge}_{0.2}\text{Te}_{0.8}\text{Se}_{0.2}$ and $(\text{Sn}_{0.85}\text{Sb}_{0.15})_{0.8}\text{Ge}_{0.2}\text{Te}_{0.8}\text{Se}_{0.2}$ samples.

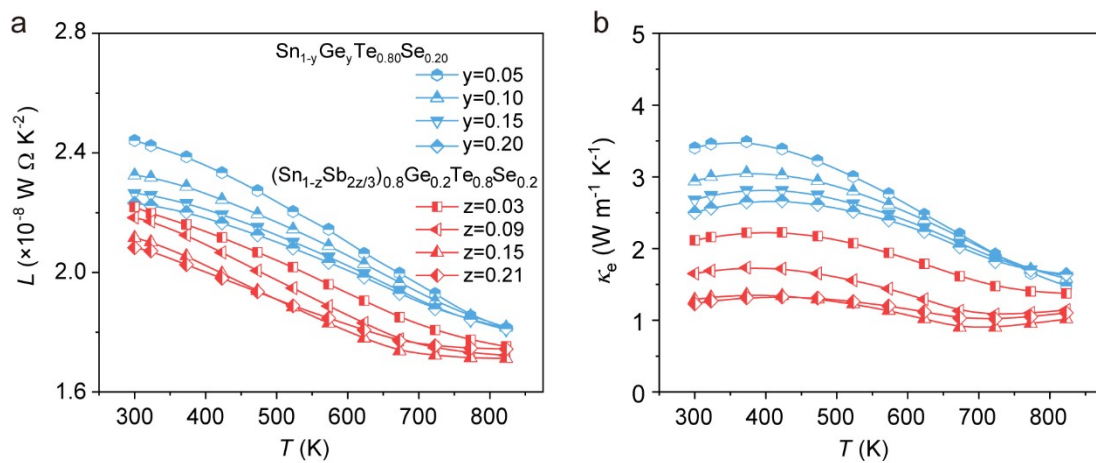


Fig. S12 T -dependent Lorentz number (a) and κ_e (b) of $\text{Sn}_{1-y}\text{Ge}_y\text{Te}_{0.8}\text{Se}_{0.2}$ ($y = 0.05, 0.10, 0.15, 0.20$) and $(\text{Sn}_{1-z}\text{Sb}_{2z/3})_{0.8}\text{Ge}_{0.2}\text{Te}_{0.8}\text{Se}_{0.2}$ ($z = 0.00, 0.03, 0.09, 0.15, \text{ and } 0.21$) samples.

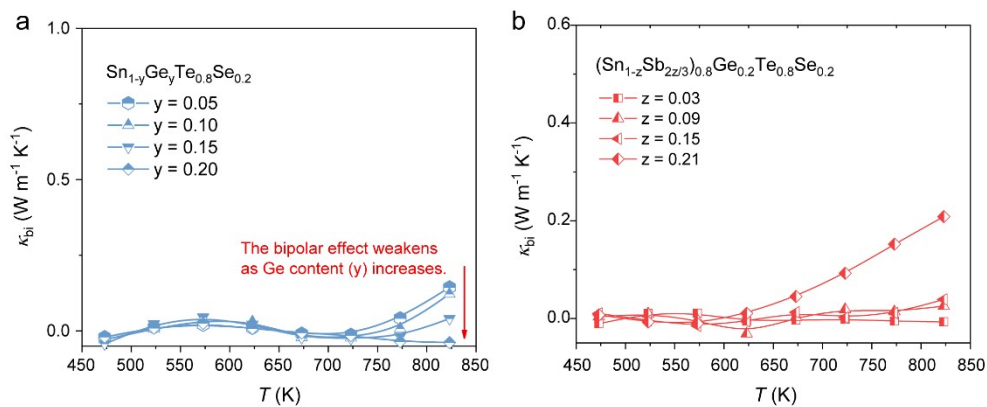


Fig. S13 T -dependent bipolar thermal conductivity (κ_{bi}) of (a) $\text{Sn}_{1-y}\text{Ge}_y\text{Te}_{0.8}\text{Se}_{0.2}$ ($y = 0.05, 0.10, 0.15, 0.20$) and (b) $(\text{Sn}_{1-z}\text{Sb}_{2z/3})_{0.8}\text{Ge}_{0.2}\text{Te}_{0.8}\text{Se}_{0.2}$ ($z = 0.03, 0.09, 0.15, \text{ and } 0.21$) samples.

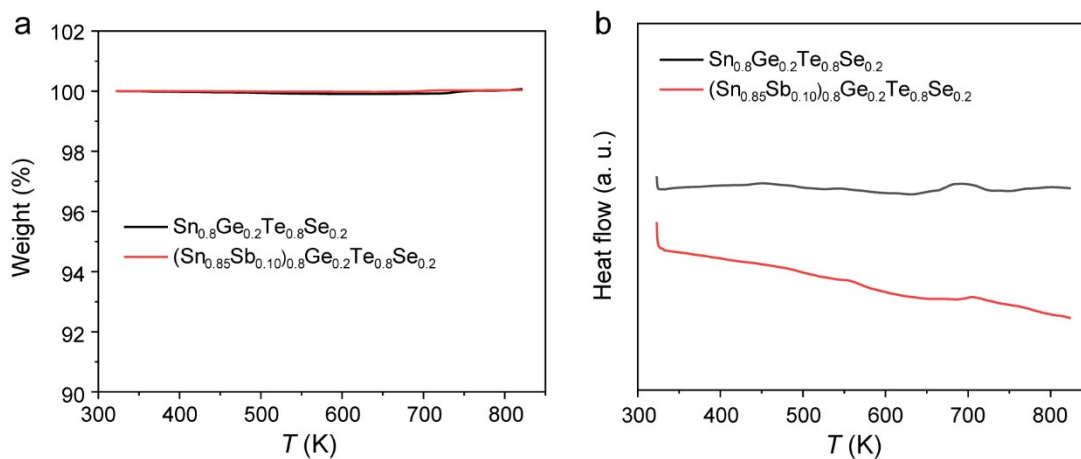


Fig. S14 The TG and DSC curves of $\text{Sn}_{0.8}\text{Ge}_{0.2}\text{Te}_{0.8}\text{Se}_{0.2}$ and $(\text{Sn}_{0.85}\text{Sb}_{0.10})_{0.8}\text{Ge}_{0.2}\text{Te}_{0.8}\text{Se}_{0.2}$ samples.

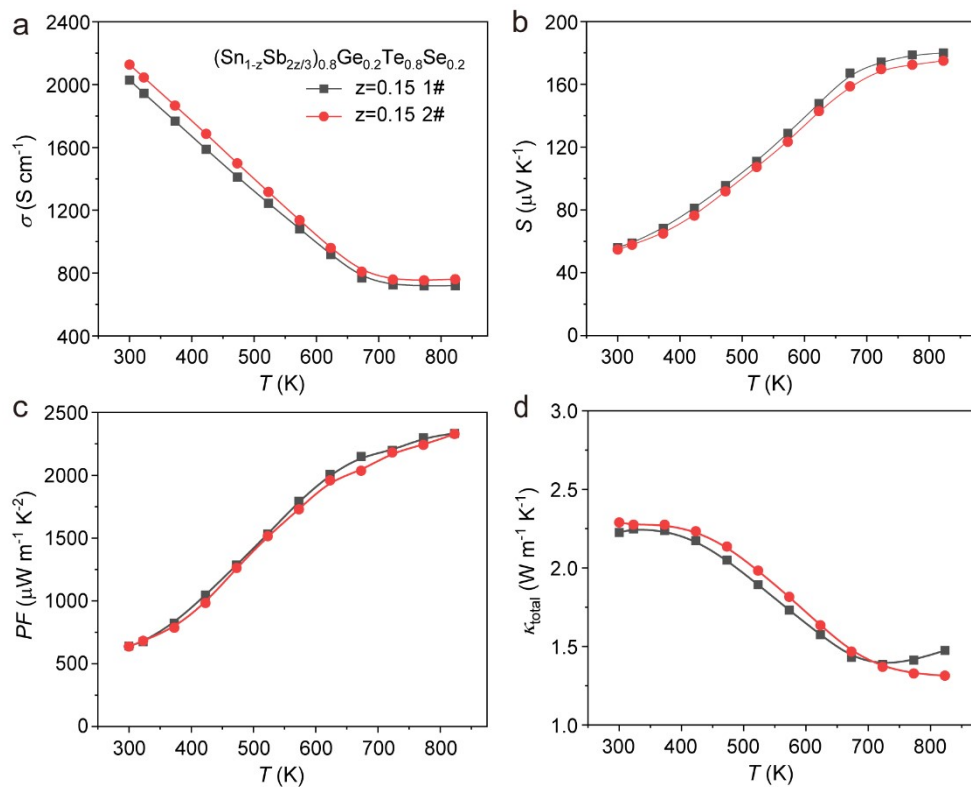


Fig. S15 The reproducible test of the $(\text{Sn}_{0.85}\text{Sb}_{0.10})_{0.8}\text{Ge}_{0.2}\text{Te}_{0.8}\text{Se}_{0.2}$ sample.

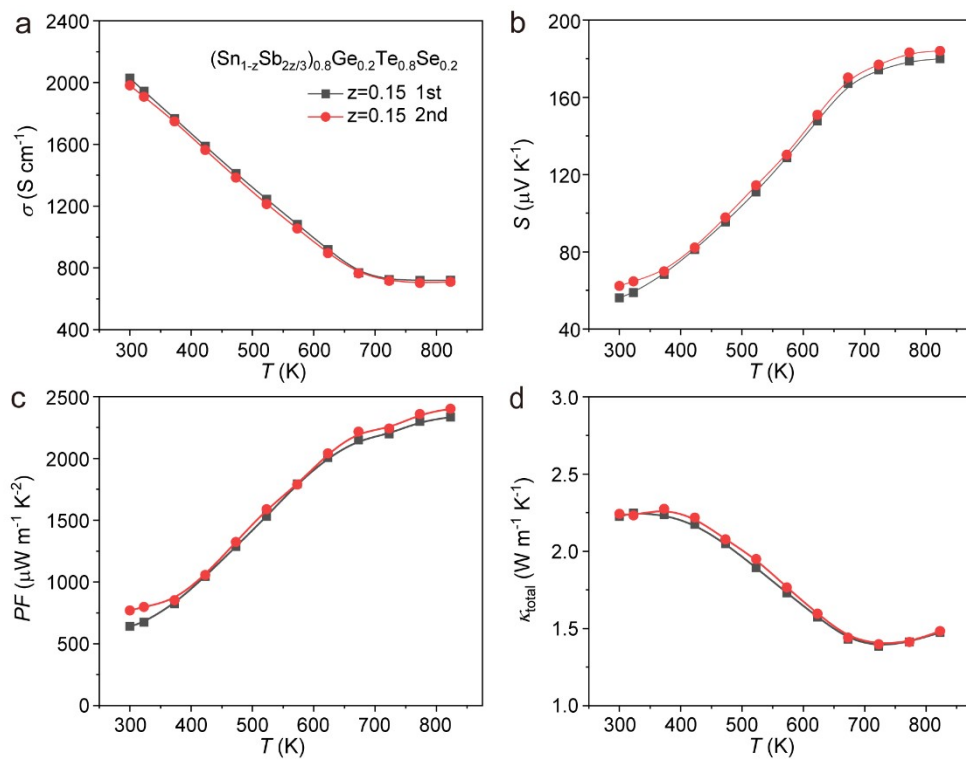


Fig. S16 Repeat tests of the $(\text{Sn}_{0.85}\text{Sb}_{0.10})_{0.8}\text{Ge}_{0.2}\text{Te}_{0.8}\text{Se}_{0.2}$ sample.

Section 2: Supplementary tables

Table S1. The density and relative density of the sintered $\text{SnTe}_{1-x}\text{Se}_x$, $\text{Sn}_{1-y}\text{Ge}_y\text{Te}_{1-x}\text{Se}_x$, and $(\text{Sn}_{1-z}\text{Sb}_{2z/3})_{0.8}\text{Ge}_{0.2}\text{Te}_{0.8}\text{Se}_{0.2}$ samples.

Sample ID	Density (g cm^{-3})	Relative density (%)
SnTe	6.435	99.5
$\text{SnTe}_{0.95}\text{Se}_{0.05}$	6.43	99.4
$\text{SnTe}_{0.90}\text{Se}_{0.10}$	6.395	98.8
$\text{SnTe}_{0.85}\text{Se}_{0.15}$	6.38	98.6
$\text{SnTe}_{0.80}\text{Se}_{0.20}$	6.385	98.7
$\text{Sn}_{0.95}\text{Ge}_{0.05}\text{Te}_{0.80}\text{Se}_{0.20}$	6.22	96.1
$\text{Sn}_{0.90}\text{Ge}_{0.10}\text{Te}_{0.80}\text{Se}_{0.20}$	6.37	98.5
$\text{Sn}_{0.85}\text{Ge}_{0.15}\text{Te}_{0.80}\text{Se}_{0.20}$	6.33	97.8
$\text{Sn}_{0.80}\text{Ge}_{0.20}\text{Te}_{0.80}\text{Se}_{0.20}$	6.31	97.5
$(\text{Sn}_{0.97}\text{Sb}_{0.02})_{0.8}\text{Ge}_{0.2}\text{Te}_{0.8}\text{Se}_{0.2}$	6.28	97.1
2	6.30	97.3
$(\text{Sn}_{0.91}\text{Sb}_{0.06})_{0.8}\text{Ge}_{0.2}\text{Te}_{0.8}\text{Se}_{0.2}$	6.31	97.5
2	6.31	97.5
$(\text{Sn}_{0.85}\text{Sb}_{0.10})_{0.8}\text{Ge}_{0.2}\text{Te}_{0.8}\text{Se}_{0.2}$		
2		
$(\text{Sn}_{0.79}\text{Sb}_{0.14})_{0.8}\text{Ge}_{0.2}\text{Te}_{0.8}\text{Se}_{0.2}$		
2		

Table S2. The formulas for relaxation times (τ) corresponding to different phonon scattering mechanisms, where τ_U^{-1} , τ_N^{-1} , τ_{PD}^{-1} , and τ_{vac}^{-1} are the relaxation times due to the scattering of Umklapp processes, Normal processes, point defects, and vacancies, respectively.

Scattering mechanisms	Relaxation times (τ)
Umklapp processes	$\tau_U^{-1} = \frac{\hbar\gamma^2}{Mv_a^2}\omega^2 T \exp(-\theta_D/3T)$ $v_a = \left[\frac{1}{3} \left(\frac{1}{v_L^3} + \frac{2}{v_T^3} \right) \right]^{-\frac{1}{3}}$
Normal processes	$\tau_N^{-1} = \beta\tau_U^{-1}$ $\tau_{PD}^{-1} = \frac{V_0\omega^4}{4\pi v_a^3}(\Gamma_M + \Gamma_S);$ $\Gamma_M = \frac{\sum_{i=1}^n c_i \left(\frac{\bar{M}_i}{\bar{M}} \right)^2 f_i^1 f_i^2 \left(\frac{M_i^1 - M_i^2}{\bar{M}_i} \right)^2}{\sum_{i=1}^n c_i};$
Point defects	$\Gamma_S = \frac{\sum_{i=1}^n c_i \left(\frac{\bar{M}_i}{\bar{M}} \right)^2 f_i^1 f_i^2 \varepsilon_i \left(\frac{r_i^1 - r_i^2}{\bar{r}_i} \right)^2}{\sum_{i=1}^n c_i};$ $\bar{M}_i = \sum_k f_i^k M_i^k;$ $\bar{M} = \frac{1}{2} \sum_{i=1}^n \bar{M}_i$
Vacancy	$\tau_{vac}^{-1} = \frac{3V_0}{G\pi v^2} s^2 \omega^4$

Table S3. Parameters used for the Debye-Callaway model simulation.

Symbol	Parameters	Value	Ref.
γ	Gruneisen parameter	2.1	5
M (kg)	Average atomic mass	$M_{\text{formula}}/(2 \times 6.022 \times 10^{23})$	calculated
v_a (m/s)	Average sound velocity	2107	exp.
θ_D (K)	Debye temperature	155	5
β	The ratio of N- to U-processes	1.7	fitted
V_0 (\AA^3)	Volume per atom	Value depends on composition	calculated
ϵ_1	Phenomenological parameter for Ge doped at Sn, Se doped at Te, respectively	5	fitted
ϵ_2		1	
M_{Sn} (g/mol)	Mole mass of Sn, Te, Ge, Se and Sb	118.71	this work
M_{Te} (g/mol)		127.6	
M_{Ge} (g/mol)		72.64	
M_{Se} (g/mol)		78.96	
M_{Sb} (g/mol)		121.76	
r_{Sn} (pm)	The radius of Sn, Te, Ge, Se and Sb atoms	132	this work
r_{Te} (pm)		207	
r_{Ge} (pm)		87	
r_{Se} (pm)		184	
r_{Sb} (pm)		90	
f_{Sn}	Fractional occupant for Sn, Te, Ge, Se and Sb in $\text{Sn}_{1-y}\text{Ge}_y\text{Te}_{1-x}\text{Se}_x$ and $(\text{Sn}_{1-z}\text{Sb}_{2z/3})_{0.8}\text{Ge}_{0.2}\text{Te}_{0.8}\text{Se}_{0.2}$	$1-y, (1-z)*0.8$	this work
f_{Te}		$1-x, 0.8$	
f_{Ge}		$y, 0.2$	
f_{Se}		$x, 0.2$	
f_{Sb}		$0, 2z/3*0.8$	
n	The number of sublattices	2	this work
k	The ordinal value of atom species at each sublattice	Sn: 1, 2; Te: 1, 2	this work
i	The ordinal value of sublattice	1, 2	this work
s^2	A measure of the vacancy scattering	0.89	3
$1/G$	The concentration of vacancy per atom	0.02 $z = 0.15$; 0.028 $z = 0.21$	calculated

Section 3: Study on the mobility of $\text{SnTe}_{1-x}\text{Se}_x$ samples

We find the $\text{SnTe}_{1-x}\text{Se}_x$ samples have similar μ values as that of single-doped SnTe materials (Fig. 3c in the main text). This result can be explained as follows. The scattering ability of one dopant on carriers depends on the mass fluctuation and strain.⁶ So, we analyzed the effect of Se doping on carrier mobility from these two perspectives. The relative mass change between Se and Te is around 38%, which is smaller than or close to those between Sn and the common cationic site dopants, such as Mn (53.7%) and Ge (39%). The strains of $\text{SnTe}_{1-x}\text{Se}_x$ samples were calculated by analyzing XRD peak broadening through a typical Williamson-Hall fitting⁷ (Fig. S17). The calculated lattice strain (ϵ) increases from 0.22% for SnTe to 0.24% for $\text{SnTe}_{0.85}\text{Se}_{0.15}$. In summary, the small mass fluctuation and tiny strain induced by Se alloying help to maintain the as high μ value for $\text{SnTe}_{1-x}\text{Se}_x$ samples as those of single-doped SnTe materials.

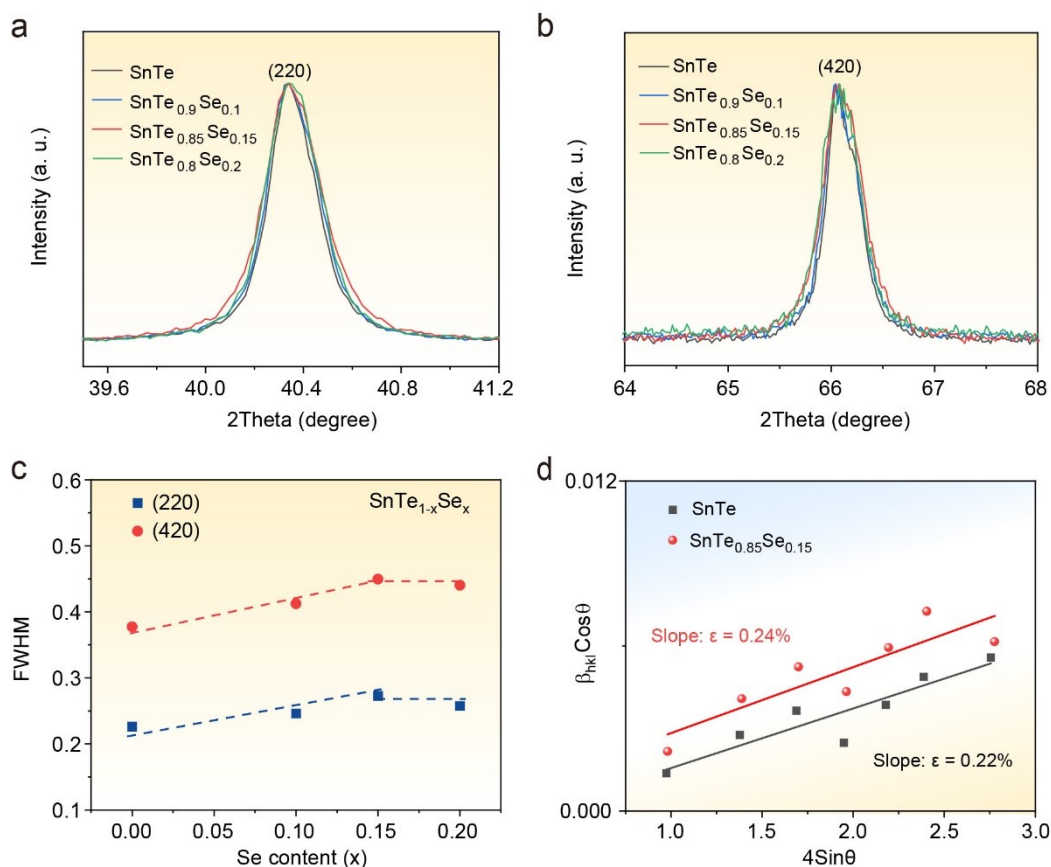


Fig. S17 (a,b) The (220) and (420) diffraction peaks for $\text{SnTe}_{1-x}\text{Se}_x$ ($x = 0.00, 0.05, 0.10, 0.15, 0.20$) samples. (c) The full width at half maximum (FWHM) of (220) and (420) peaks for $\text{SnTe}_{1-x}\text{Se}_x$ ($x = 0.00, 0.05, 0.10, 0.15, 0.20$) samples. (d) The calculated lattice strain by a typical Williamson-Hall fitting for all diffraction peaks of SnTe and $\text{SnTe}_{0.85}\text{Se}_{0.15}$ samples. The β_{hkl} value is the FWHM of the (hkl) peak.

Section 4: Density functional theory calculation.

The vibration entropy (S_{vib}) and electronic structure were both performed through density functional theory within projected augmented wave (PAW) method⁸ and generalized gradient approximation reported by Perdew, Burke, and Ernzerhof (GGA-PBE)⁹ for exchange correlation functional.^{10,11} To obtain the SnTe-based high-entropy structure for S_{vib} calculation, a series of $2 \times 2 \times 2$ supercells (containing 64 atoms) with special quasi-random structures were constructed via alloy theoretic automated toolkit (ATAT) code.⁵ A series of $4 \times 4 \times 4$ high-entropy supercells (containing 128 atoms) expanded from the SnTe primitive cell are used for calculating the electron density of states (DOS) and unfolded band structure for Se alloyed and high-entropy SnTe, respectively.

The energy cutoff was set to 400 eV for all following calculations. During structure relaxation, the convergence precision of Hellman-Feynman force was smaller than 10^{-5} eV/Å⁻¹. The relaxed lattice parameters are within an error of 2% from each sample's experimental values (Table S4). The Brillouin-zone sampling was performed on Monkhorst–Pack meshes⁶ except for S_{vib} and DOS calculation, which are calculated by using a Γ -centered k-mesh and tetrahedron method with Blöchl corrections.⁷ The second order force constants matrices of a series of high entropy structure were calculated⁸ through density functional perturbation theory (DFPT).⁹ Using the Phonopy code for post-processing, we got S_{vib} and other thermal properties at 300 K. The spin orbit coupling (SOC) effect were considered in all electronic structures. DOS and band structure data were extracted via VASPKIT code.¹²

Usually, there are three methods to carry out the construction of high entropy alloys (HEA), which are special quasi-random structure (SQS),^{13,14} cluster plus approximation (CPA),^{15,16} and supercell method.¹⁷ SQS method optimizes the atomic arrangement by minimizing the interatomic correlation function, which preserves the short-range ordered structure and can more accurately reflect the chemical environment of the system.

To date, researchers have performed a series of calculations on the formation energies,¹⁸ elastic properties,¹⁹ bond length distributions,²⁰ and electronic structures^{21,22} of HEAs by supercells constructed by the SQS method, which are in good agreement with the experimental results. We performed structural search of high entropy alloys with different components by Monte Carlo-SQS tool^{23,24} and used the best-searched structure, all of which have the lowest symmetry (P1 space group).

Through structural relaxation by DFT, we optimized both the lattice parameters and atomic positions to keep the internal lattice stresses as small as possible in order to obtain a more stable and realistic HEA structure.

By XRD refinement, we obtained the experimental lattice parameters. The Rietveld structure refinements of studied samples are conducted by FullProf software²⁵ and the results of two typical samples are shown in Fig. S18. The lattice parameters obtained from DFT calculations are shown in Table S4 in comparison with their counterparts. The relative error is within 2%, which is acceptable.²⁶ Both experimental and theoretical values show that the cell parameters decrease with the increase of solid solubility.

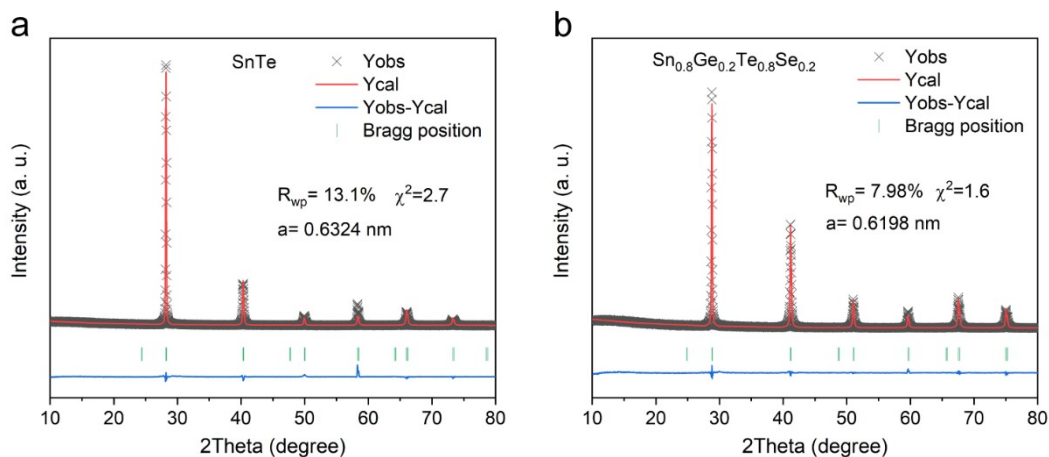


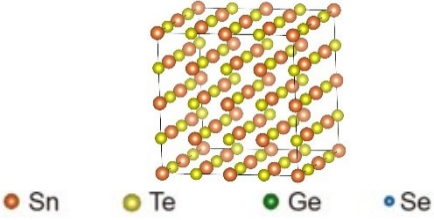
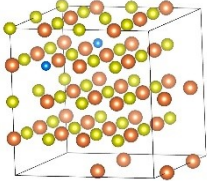
Fig. S18 The Rietveld structure refinement results of two typical samples: SnTe and $\text{Sn}_{0.8}\text{Ge}_{0.2}\text{Te}_{0.8}\text{Se}_{0.2}$.

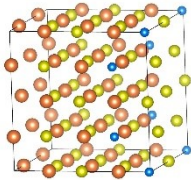
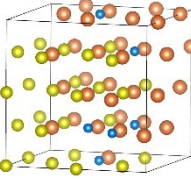
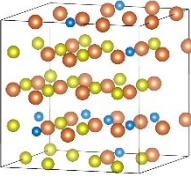
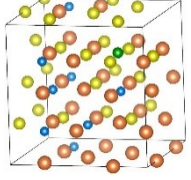
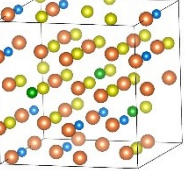
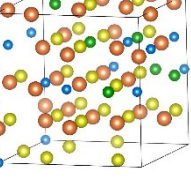
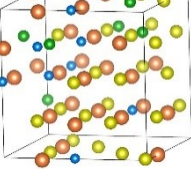
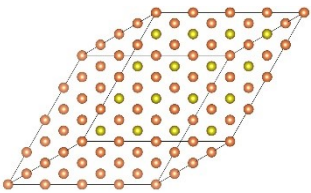
In the construction of the SQS structure, we try to make the content of each element as close as possible to the experimental value, and the relevant data are shown in Table S5. For Gibbs free energy calculations, we constructed $2 \times 2 \times 2$ SQS supercells from conventional cell of SnTe, containing a total of 64 atoms. For electronic structure calculations, we constructed $4 \times 4 \times 4$ SQS supercells from the primitive cell of SnTe, which contain 128 atoms. Referring to the search principle of SQS²⁷ with some high-level computational papers on high-entropy alloys,²² our supercells are large enough for the relevant computational needs.

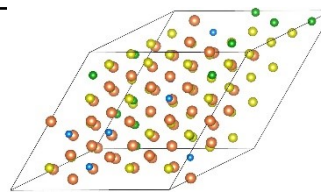
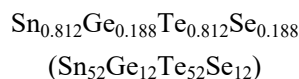
Table S4. Comparison of experimental and calculated lattice parameters (normalized).

Nominal component	Lattice parameter obtained by Rietveld refinement (a=b=c, Å)	Lattice parameter obtained by relaxation calculation (a=b=c, Å)	Relative error
Structures for Gibbs free energy calculation			
SnTe	6.324	6.412	1.39%
SnTe _{0.95} Se _{0.05}	6.313	6.402	1.41%
SnTe _{0.90} Se _{0.10}	6.296	6.384	1.40%
SnTe _{0.15} Se _{0.15}	6.278	6.368	1.43%
SnTe _{0.80} Se _{0.20} (nonholomorphic)	6.268	6.351	1.32%
Sn _{0.95} Ge _{0.05} Te _{0.80} Se _{0.20} (nonholomorphic)	6.249	6.341	1.47%
Sn _{0.90} Ge _{0.10} Te _{0.80} Se _{0.20}	6.232	6.318	1.38%
Sn _{0.85} Ge _{0.15} Te _{0.80} Se _{0.20}	6.214	6.301	1.40%
Sn _{0.80} Ge _{0.20} Te _{0.80} Se _{0.20}	6.198	6.278	1.29%
Structures for electronic structure calculation			
SnTe	6.324	6.412	1.39%
Sn _{0.80} Ge _{0.20} Te _{0.80} Se _{0.20}	6.198	6.306	1.74%

Table S5. Structure and chemical formula for Gibbs free energy and electronic structure calculation.

Experimental component (Nominal component)	Chemical formula of supercell	Supercell structure
Structures for Gibbs free energy calculation		
SnTe	SnTe (Sn ₃₂ Te ₃₂)	
SnTe _{0.95} Se _{0.05}	SnTe _{0.969} Se _{0.031} (Sn ₃₂ Te ₃₁ Se ₁)	

$\text{SnTe}_{0.90}\text{Se}_{0.10}$	$\text{SnTe}_{0.906}\text{Se}_{0.094}$ ($\text{Sn}_{32}\text{Te}_{29}\text{Se}_3$)	
$\text{SnTe}_{0.15}\text{Se}_{0.15}$	$\text{SnTe}_{0.843}\text{Se}_{0.156}$ ($\text{Sn}_{32}\text{Te}_{27}\text{Se}_5$)	
$\text{SnTe}_{0.80}\text{Se}_{0.20}$ (nonholomorphic)	$\text{SnTe}_{0.781}\text{Se}_{0.219}$ ($\text{Sn}_{32}\text{Te}_{25}\text{Se}_7$)	
$\text{Sn}_{0.95}\text{Ge}_{0.05}\text{Te}_{0.80}\text{Se}_{0.20}$ (nonholomorphic)	$\text{Sn}_{0.969}\text{Ge}_{0.031}\text{Te}_{0.781}\text{Se}_{0.219}$ ($\text{Sn}_{31}\text{Ge}_1\text{Te}_{25}\text{Se}_7$)	
$\text{Sn}_{0.90}\text{Ge}_{0.10}\text{Te}_{0.80}\text{Se}_{0.20}$	$\text{Sn}_{0.906}\text{Ge}_{0.094}\text{Te}_{0.781}\text{Se}_{0.219}$ ($\text{Sn}_{29}\text{Ge}_3\text{Te}_{25}\text{Se}_7$)	
$\text{Sn}_{0.85}\text{Ge}_{0.15}\text{Te}_{0.80}\text{Se}_{0.20}$	$\text{Sn}_{0.843}\text{Ge}_{0.156}\text{Te}_{0.781}\text{Se}_{0.219}$ ($\text{Sn}_{27}\text{Ge}_5\text{Te}_{25}\text{Se}_7$)	
$\text{Sn}_{0.80}\text{Ge}_{0.20}\text{Te}_{0.80}\text{Se}_{0.20}$	$\text{Sn}_{0.781}\text{Ge}_{0.219}\text{Te}_{0.781}\text{Se}_{0.219}$ ($\text{Sn}_{25}\text{Ge}_7\text{Te}_{25}\text{Se}_7$)	
Structures for electronic structure calculation		
SnTe	SnTe ($\text{Sn}_{64}\text{Te}_{64}$)	



References

- 1 J. He, L.-D. Zhao, J.-C. Zheng, J. W. Doak, H. Wu, H.-Q. Wang, Y. Lee, C. Wolverton, M. G. Kanatzidis and V. P. Dravid, *J. Am. Chem. Soc.*, 2013, **135**, 4624-4627.
- 2 S.-H. Lo, J. He, K. Biswas, M. G. Kanatzidis and V. P. Dravid, *Adv. Funct. Mater.*, 2012, **22**, 5175-5184.
- 3 G. Tan, S. Hao, R. C. Hanus, X. Zhang, S. Anand, T. P. Bailey, A. J. E. Rettie, X. Su, C. Uher, V. P. Dravid, G. J. Snyder, C. Wolverton and M. G. Kanatzidis, *ACS Energy Lett.*, 2018, DOI: 10.1021/acsenergylett.8b00137, 705-712.
- 4 C. A. Ratsifaritana and P. G. Klemens, *Int. J. Thermophys.*, 1987, **8**, 737-750.
- 5 E. S. Toberer, A. Zevalkink and G. J. Snyder, *J. Mater. Chem.*, 2011, **21**, 15843-15852.
- 6 Z. Chen, X. Zhang and Y. Pei, *Advanced Materials*, 2018, **30**, 1705617.
- 7 V. D. Mote, Y. Purushotham and B. N. Dole, *J. Theor. Appl. Phys.*, 2012, **6**, 6.
- 8 P. E. Blöchl, *Phys. Rev. B*, 1994, **50**, 17953-17979.
- 9 J. P. Perdew, K. Burke and M. Ernzerhof, *Phys. Rev. Lett.*, 1996, **77**, 3865-3868.
- 10 G. Kresse and J. Furthmüller, *Phys. Rev. B*, 1996, **54**, 11169-11186.
- 11 G. Kresse and D. Joubert, *Phys. Rev. B*, 1999, **59**, 1758-1775.
- 12 V. Wang, N. Xu, J.-C. Liu, G. Tang and W.-T. Geng, *Computer Physics Communications*, 2021, **267**, 108033.
- 13 S. H. Wei, L. G. Ferreira, J. E. Bernard and A. Zunger, *Phys. Rev. B*, 1990, **42**, 9622-9649.
- 14 A. Zunger, S. H. Wei, L. G. Ferreira and J. E. Bernard, *Phys. Rev. Lett.*, 1990, **65**, 353-356.
- 15 P. Soven, *Phys. Rev.*, 1967, **156**, 809-813.
- 16 G. M. Stocks, W. M. Temmerman and B. L. Gyorffy, *Phys. Rev. Lett.*, 1978, **41**, 339-343.
- 17 Y. Wang, G. M. Stocks, W. A. Shelton, D. M. C. Nicholson, Z. Szotek and W. M. Temmerman, *Phys. Rev. Lett.*, 1995, **75**, 2867-2870.
- 18 M. C. Gao, Y. Suzuki, H. Schweiger, Ö. N. Doğan, J. Hawk and M. Widom, *J. Phys.: Condens. Matter*, 2013, **25**, 075402.
- 19 F. Tasnádi, M. Odén and I. A. Abrikosov, *Phys. Rev. B*, 2012, **85**, 144112.
- 20 Z. W. Lu, S. H. Wei and A. Zunger, *Phys. Rev. B*, 1992, **45**, 10314-10330.
- 21 M. Hong, W. Lyv, M. Li, S. Xu, Q. Sun, J. Zou and Z.-G. Chen, *Joule*, 2020, **4**, 2030-2043.

- 22 B. Jiang, Y. Yu, J. Cui, X. Liu, L. Xie, J. Liao, Q. Zhang, Y. Huang, S. Ning, B. Jia, B. Zhu, S. Bai, L. Chen, J. Pennycook Stephen and J. He, *Science*, 2021, **371**, 830-834.
- 23 A. van de Walle, M. Asta and G. Ceder, *Calphad*, 2002, **26**, 539-553.
- 24 A. van de Walle, P. Tiwary, M. de Jong, D. L. Olmsted, M. Asta, A. Dick, D. Shin, Y. Wang, L. Q. Chen and Z. K. Liu, *Calphad*, 2013, **42**, 13-18.
- 25 J. Rodríguez-Carvajal, *Physica B: Condensed Matter*, 1993, **192**, 55-69.
- 26 K. Lejaeghere, G. Bihlmayer, T. Björkman, P. Blaha, S. Blügel, V. Blum, D. Caliste, I. E. Castelli, S. J. Clark, A. Dal Corso, S. de Gironcoli, T. Deutsch, J. K. Dewhurst, I. Di Marco, C. Draxl, M. Dułak, O. Eriksson, J. A. Flores-Livas, K. F. Garrity, L. Genovese, P. Giannozzi, M. Giantomassi, S. Goedecker, X. Gonze, O. Grånäs, E. K. U. Gross, A. Gulans, F. Gygi, D. R. Hamann, P. J. Hasnip, N. A. W. Holzwarth, D. Iuşan, D. B. Jochym, F. Jollet, D. Jones, G. Kresse, K. Koepf, E. Küçükbenli, Y. O. Kvashnin, I. L. M. Locht, S. Lubeck, M. Marsman, N. Marzari, U. Nitzsche, L. Nordström, T. Ozaki, L. Paulatto, C. J. Pickard, W. Poelmans, M. I. J. Probert, K. Refson, M. Richter, G.-M. Rignanese, S. Saha, M. Scheffler, M. Schlipf, K. Schwarz, S. Sharma, F. Tavazza, P. Thunström, A. Tkatchenko, M. Torrent, D. Vanderbilt, M. J. van Setten, V. Van Speybroeck, J. M. Wills, J. R. Yates, G.-X. Zhang and S. Cottenier, *Science*, 2016, **351**, aad3000.
- 27 M. Karabin, W. R. Mondal, A. Östlin, W.-G. D. Ho, V. Dobrosavljevic, K.-M. Tam, H. Terletska, L. Chioncel, Y. Wang and M. Eisenbach, *J. Mater. Sci.*, 2022, **57**, 10677-10690.